

# Modeling laser-induced periodic surface structures: Finite-difference time-domain feedback simulations

J. Z. P. Skolski,<sup>1,a)</sup> G. R. B. E. Römer,<sup>2</sup> J. Vincenc Obona,<sup>1</sup> and A. J. Huis in 't Veld<sup>2</sup>

<sup>1</sup>Materials innovation institute M2i, Faculty of Engineering Technology, Chair of Applied Laser Technology, University of Twente, P.O. Box 217, 7500 AE Enschede, The Netherlands

<sup>2</sup>Faculty of Engineering Technology, Chair of Applied Laser Technology, University of Twente, P.O. Box 217, 7500 AE Enschede, The Netherlands

(Received 7 December 2013; accepted 24 February 2014; published online 11 March 2014)

A model predicting the formation of laser-induced periodic surface structures (LIPSSs) is presented. That is, the finite-difference time domain method is used to study the interaction of electromagnetic fields with rough surfaces. In this approach, the rough surface is modified by “ablation after each laser pulse,” according to the absorbed energy profile, in order to account for inter-pulse feedback mechanisms. LIPSSs with a periodicity significantly smaller than the laser wavelength are found to “grow” either parallel or orthogonal to the laser polarization. The change in orientation and periodicity follow from the model. LIPSSs with a periodicity larger than the wavelength of the laser radiation and complex superimposed LIPSS patterns are also predicted by the model. © 2014 AIP Publishing LLC. [<http://dx.doi.org/10.1063/1.4867759>]

## I. INTRODUCTION

Laser-induced periodic surface structures (LIPSSs) have been observed and studied since 1965;<sup>1</sup> however, a complete understanding of their origin and growth is still missing. The most common LIPSSs, also referred to as ripples, consist of wavy surfaces, which can be produced on metals,<sup>2–4</sup> semiconductors,<sup>5–7</sup> and dielectrics.<sup>8,9</sup> When created with linearly polarized laser radiation at normal incidence, these ripples have a periodicity close to the laser wavelength  $\lambda$ , and their direction is orthogonal to the polarization of the laser light. Ripples showing these properties can be produced with either continuous wave lasers<sup>10</sup> or pulsed lasers<sup>2–7</sup> and are usually referred to as low spatial frequency LIPSSs (LSFLs). It is generally accepted that LSFL formation is driven by the interaction of electromagnetic fields with the rough surface of materials.<sup>5,8,11</sup> The Sipe theory is commonly considered to be the most adequate description of this interaction.<sup>11</sup>

The observation of ripples with a periodicity significantly smaller than the laser light, referred to as high spatial frequency LIPSSs (HSFLs), renewed interest in the topic since the early 2000s.<sup>3,4,12–15</sup> HSFLs attracted attention for mainly two reasons. First, from a practical point of view, HSFLs show a strong potential for nanostructuring due to their small dimensions. While, from a theoretical point of view, the electromagnetic theory adopted by Sipe fails to explain HSFL formation. As for LSFLs, HSFLs have been observed on metals,<sup>3,4,12</sup> semiconductors,<sup>13–15</sup> and dielectrics.<sup>9,16</sup> Unlike LSFLs, HSFLs can be oriented both parallel<sup>3,4,9,14</sup> or orthogonal<sup>12,13,15,16</sup> to the laser beam polarization. Moreover, HSFLs have been observed for laser pulse durations in the picosecond and femtosecond regime only.

The origin of HSFL is still under debate and several theories have been proposed to explain their formation. That is,

several authors proposed extensions of the electromagnetic approach, such as second harmonic generation (SHG),<sup>13</sup> variation of the optical properties of the material during the pulse,<sup>9</sup> or both.<sup>15</sup> While these extensions were able to explain features of HSFLs in some cases, the plethora of unexplained LIPSSs<sup>3,4,14</sup> led to another approach. That is, it was proposed that LIPSSs are the result of “self-organization from an instability induced by the ablation process.”<sup>14,16,17</sup> However, none of the above mentioned theories can explain all characteristics of HSFLs.

In a recent article,<sup>18</sup> the interaction of electromagnetic waves with the rough surface of materials was investigated numerically based on the finite-difference time-domain (FDTD) method and compared to the Sipe theory.<sup>11</sup> A good agreement was found in most cases, but it was shown that the Sipe theory fails to predict few important features. It was also stressed that the FDTD method could be used to study qualitatively the effect of inter-pulse feedback mechanisms on LIPSS formation. The latter is the subject of this article.

In the first part of this article, a new model combining the FDTD method and inter-pulse feedback mechanisms is presented. This approach is referred to as “FDTD-feedback” simulations. In the second part, the results of the FDTD-feedback simulations are shown and compared to observations of LIPSSs reported in literature.

## II. DESCRIPTION OF THE MODEL

Figure 1 visualizes the basic idea of the FDTD-feedback simulations. That is, in the simulations, the incident laser radiation interacts with the rough surface and the absorbed energy  $A(x, y, z)$  in the material, resulting from this interaction, is calculated based on the FDTD method, as will be explained in Sec. II B. Once  $A(x, y, z)$  is known, an isoline of absorbed energy,  $A(x, y, z) = A_{\text{ablation}}$ , is selected. This isoline is assumed to correspond to the threshold at which the ablation of material occurs. Next, the shape of the rough surface is

<sup>a)</sup>Electronic mail: [j.z.p.skolski@utwente.nl](mailto:j.z.p.skolski@utwente.nl)

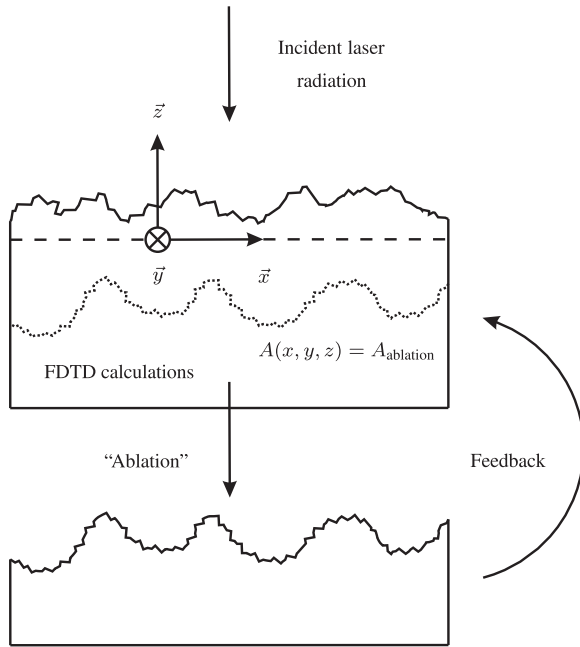


FIG. 1. Steps followed in the FDTD-feedback simulations.

modified (updated) by material removal (“Ablation”). That is, all the material above the chosen isoline is “removed” from the simulation domain. Hence, the new surface morphology follows the isoline, and it can be used for subsequent FDTD simulation, leading to a new absorbed energy profile and a further modification of the surface. The FDTD-feedback cycle can be iterated as many times as necessary. This approach allows to study qualitatively the inter-pulse feedback mechanisms involved in LIPSS formation. It should be noted that the outcome of this approach is influenced by the choice of the nonphysical ablation threshold.

### A. Scope of the FDTD-feedback simulations

It is impractical to perform FDTD-feedback simulations for all combinations of wavelengths of the laser radiation, polarization states, initial rough surfaces, or optical properties of the material. This section defines the scope of the FDTD-feedback simulations presented in this article.

The laser radiation was modeled as a plane wave of wavelength  $\lambda = 800$  nm, linearly polarized along the  $\vec{x}$  axis and arriving at normal incidence to the rough surface. This limitation does not significantly hinder the comparison of the modeling results with literature. In fact, the femtosecond laser sources which are the most frequently used to produce LIPSSs operate under these conditions.

The optical properties of the media, chosen to demonstrate the merits of the FDTD-feedback simulations, are computed using the same approach as Bonse *et al.* while testing the Sipe Drude model on silicon.<sup>7</sup> That is, the optical properties of the excited silicon are computed via the complex permittivity  $\tilde{\epsilon}^* = \tilde{\epsilon} + \Delta\tilde{\epsilon}_{\text{Drude}}$ , where  $\Delta\tilde{\epsilon}_{\text{Drude}}$  is given by

$$\Delta\tilde{\epsilon}_{\text{Drude}} = \frac{-e^2 N_e}{\epsilon_0 m_{\text{opt}}^* m_e \omega^2 (1 + i(\omega\tau_D)^{-1})}. \quad (1)$$

$e$ ,  $N_e$ ,  $m_{\text{opt}}^*$ ,  $m_e$ ,  $\omega$ , and  $\tau_D$  are, respectively, the electron charge, the electron density in the conduction band, the optical effective mass of the carriers, the free electron mass, the angular frequency, and Drude damping time. The values  $m_{\text{opt}}^* = 0.18$  and  $\tau_D = 1.1$  fs for femtosecond-laser-excited silicon were chosen in accordance with the work of Bonse *et al.*<sup>7</sup> as well as the optical properties of unexcited silicon  $\tilde{n} = \sqrt{\tilde{\epsilon}} = 3.692 + 0.0065j$ , where  $\tilde{n}$  and  $\tilde{\epsilon}$  are the complex refractive index and the permittivity of unexcited silicon at  $\lambda = 800$  nm, respectively. The complex refractive index of the excited material  $\tilde{n}^* = \sqrt{\tilde{\epsilon}^*}$  is indicated when necessary. It is worth noting that the optical properties are assumed constant during one run of the FDTD-feedback simulation. The reasons for this choice of optical properties are various. First, LIPSSs on silicon have been studied extensively.<sup>7,14,19</sup> Second, the values used in Eq. (1) were carefully determined by Sokolowski-Tinten and Von der Linde.<sup>20</sup> Finally, the Sipe-Drude model<sup>7</sup> and previous FDTD calculations were presented with these optical properties.<sup>18,21</sup>

At the start of any FDTD-feedback simulation, a rough surface needs to be defined. In this article, all the FDTD-feedback simulations were performed starting from a  $20 \times 20 \mu\text{m}^2$  rough surface, constituted of “bumps” randomly distributed and with a height small compared to the laser wavelength. This kind of roughness is characteristic for the Sipe theory.<sup>11</sup> It is particularly interesting from a theoretical point of view since the frequency spectrum of such a roughness is almost “flat;” therefore, the interaction of electromagnetic waves with the rough surface is not biased by the geometry of the latter.<sup>21</sup> A more detailed description of the initial rough surface is presented in Sec. II B.

### B. FDTD method

The FDTD method originates from Yee in 1966.<sup>22</sup> The Yee algorithm solves, for both the electric field  $\vec{E}$  and the magnetic field  $\vec{H}$ , the time dependent Maxwell’s curl equations in differential form. That is, Ampere’s law and Faraday’s laws are discretized using central-difference approximations for both the time and space derivatives. An extensive presentation of the Yee algorithm and its extension to handle lossy or dispersive media is well described in literature.<sup>23</sup> Therefore, this is out of the scope of this article. Instead, this section is used to summarize the FDTD features which are necessary to perform the FDTD-feedback simulations.

In Fig. 2, the simulation domain is represented at the start of the FDTD-feedback simulations. The dimensions of the different parts of the simulation domain are indicated in terms of number of Yee cells (yc), which is the unit cell in the Yee algorithm. The Yee cells used for the computations had the following dimensions:  $\Delta x = \Delta y = 20$  nm and  $\Delta z = 5$  nm. These values were chosen to satisfy two criteria: perform accurate (and numerically stable) FDTD simulations and keep the demand on the computer resources reasonable, in terms of speed and memory. With the optical properties defined in Sec. II A, the smallest wavelength “traveling” in the simulation domain is equal to  $\lambda/\text{Re}(\tilde{n}) = 800/3.692 \approx 217$  nm. It was shown empirically

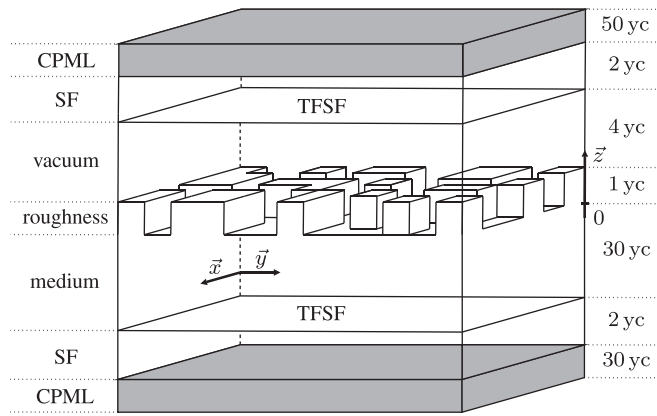


FIG. 2. Simulation domain used at the start of FDTD-feedback simulations. The dimensions of each part of the simulation domain are indicated in terms of Yee cells.

that 10 Yee cells per wavelength lead to accurate results;<sup>23</sup> hence, 20 nm is valid for the lateral dimensions of the Yee cell. In the vertical direction, 5 nm was chosen as the size of the Yee cell since the amplitude of the absorbed energy in the material can decrease rapidly from the surface. The time increment  $\Delta t = 1.5 \times 10^{-17}$  s was chosen to satisfy the stability criteria, also referred to as Courant-Friedrichs-Lewy condition, derived by Taflove and Brodwin.<sup>24</sup>

At the start of the simulation, the rough surface occupies only the plane just above  $z = 0$ . Hence the maximum height of the bumps is equal to 5 nm, which is small compared to the laser wavelength. Random numbers are used to determine which parts of the rough surface are occupied by material or vacuum. Ten percent of this plane was filled by material at the start of the FDTD-feedback simulations, which is a value commonly chosen in the case of the Sipe theory.<sup>6,7,18</sup> Below this plane, 30 yc, that is, 150 nm of material is available to compute the absorbed energy. Above the rough surface, vacuum is assumed.

The plane wave is introduced in the simulation domain by the total-field scattered-field (TFSF) technique.<sup>23</sup> In the total-field region (TF), all the computations of interest for this article occur, while in the scattered-field (SF) regions, convolutional perfectly matched layers (CPMLs) were implemented.<sup>23,25</sup> The CPMLs are of great importance since these allow to simulate semi-infinitely extended media. Indeed, if these kind of boundary layers are not implemented, nonphysical reflections occur at the edges of the simulation grid. In the  $\vec{x}$  and  $\vec{y}$  directions, periodic boundary conditions are used due to the nature of the studied phenomenon.<sup>23</sup>

The algorithm chosen for the FDTD calculations depends on the optical properties of the medium. In cases where  $\text{Re}(\tilde{n}^*) > \text{Im}(\tilde{n}^*)$ , the Yee algorithm, extended to handle lossy media, was used.<sup>23</sup> If  $\text{Re}(\tilde{n}^*) \leq \text{Im}(\tilde{n}^*)$ , the Yee algorithm is unstable<sup>26,27</sup> and the auxiliary differential equation method was used.<sup>23</sup>

### C. Feedback by “ablation”

Inter-pulse feedback mechanisms leading to LIPSS formation are complex. In the case of nanosecond laser pulses, for example, different melting regimes, during which LSFLs

form, have been identified by Young *et al.*<sup>28</sup> In the case of ultra-short laser pulses, that is, femtosecond and picosecond laser pulses, such a study is missing, but ablation seems to play a key role regarding the growth of LIPSSs.<sup>29–31</sup> A detailed modeling of the mechanisms governing the transport of molten or ablated material is not only complex but also out of the scope of this article. Instead, a simplified approach was chosen to account for inter-pulse feedback mechanisms as presented in Fig. 1. This approach is referred to as the holographic ablation model (HAM). It is worth noting that the term “holographic” was used in a recent article<sup>32</sup> to refer to the Sipe theory<sup>11</sup> and the work of Young *et al.*<sup>6,28</sup>

As mentioned earlier, while discussing Fig. 1, the constant  $A_{\text{ablation}}$  is an additional parameter which needs to be chosen carefully. The ablation threshold of a material can be determined experimentally.<sup>33</sup> However, an exact value would be of little use in the HAM because the intra-pulse feedback is included in the FDTD calculations only qualitatively. That is, the optical properties are kept constant during one FDTD simulation, in accordance with the number of electrons in the conduction band and the Sipe-Drude model.<sup>7</sup> Similarly, the dynamics of the carriers, the electron, and the lattice temperatures of the material are not incorporated. Hence, no quantitative prediction of the absorbed energy is possible; therefore,  $A_{\text{ablation}}$  should be determined differently. Prior to any FDTD-feedback simulation, a FDTD simulation, with identical parameters, is used to calculate the absorbed energy below a flat surface. At a certain depth, the absorbed energy  $A_{\text{ablation}}$  necessary to remove a thickness of material, referred to as ablation depth  $\Delta_{\text{ablation}}$ , is determined and stored to perform the feedback step in the FDTD-feedback simulations. That is, the removal of material required to create the new surface roughness. Since there is a bijection between  $A_{\text{ablation}}$  and  $\Delta_{\text{ablation}}$ , for constant simulation parameters,  $\Delta_{\text{ablation}}$  is employed to refer to the simulations presented in this article. It is worth noting that, in the FDTD-feedback simulations,  $\Delta_{\text{ablation}}$  is a parameter as well as the number of electrons in the conduction band  $N_e$ . However, in experiments, a qualitative relationship exists: a high laser fluence leads to large values of  $N_e$  and  $\Delta_{\text{ablation}}$ , where the exact magnitude depends on the material. The FDTD-feedback simulations treat these two quantities as if they were decoupled, since the relation between  $N_e$  and  $\Delta_{\text{ablation}}$  is too complex to be included quantitatively in the model. This is not always a drawback, since this decoupling allows to investigate hypothetical materials. Hence, it allows to discuss the results of the FDTD-feedback simulations for other materials than silicon only.

One last limitation of the HAM concerns all the phenomena related to incubation.<sup>2</sup> That is, the fluence threshold for which a certain kind of morphology, i.e., LIPSS, occur decreases with the number of applied laser pulses. This accumulative behavior is out of the scope of the FDTD-feedback simulations. The main outcome of working with the non-physical ablation threshold is that LIPSSs grow after less cycles (“pulses”) in this model than in reality. All the results presented in Sec. III were computed with a maximum of nine FDTD-feedback cycles, which was sufficient to obtain well developed LIPSS patterns.



### III. SIMULATION RESULTS

In this section, the results of the FDTD-feedback simulations are presented. First, an overview of the kind of LIPSSs predicted by the simulations is given in Sec. III A. Next, critical aspects of LIPSS formation are addressed through Sec. III B to Sec. III E, namely, the variation of the periodicity of LSFLs in Sec. III B, the variation of the properties of HSFLs orthogonal to the polarization in Sec. III C, the formation of HSFLs parallel to the polarization on metals in Sec. III D, and the presence of superimposed LIPSS patterns in Sec. III E. Finally, the specific frequency domain signature of each LIPSS is shown in Sec. III F.

#### A. Overview

It would be impractical to show the results of FDTD-feedback simulations for each set of  $(N_e, \Delta_{\text{ablation}})$ . Instead, a “map” indicating which kind of LIPSSs is predicted by the model, depending on  $(N_e, \Delta_{\text{ablation}})$ , is presented in Fig. 3.

This map was compiled by observing the LIPSSs obtained after nine FDTD-feedback simulations for each set of parameters  $(N_e, \Delta_{\text{ablation}})$ , with  $N_e = [2, 10] \times 10^{27} \text{ m}^{-3}$  and  $20 \text{ nm} \leq \Delta_{\text{ablation}} \leq 50 \text{ nm}$  with steps of 5 nm. It is worth noting that the solid lines delimiting the different “regions” of the map are not strict boundaries. That is, a more detailed map would show transition zones. The absence of simulations is shown by the hatched areas in the map. The upper limit  $\Delta_{\text{ablation}} = 50 \text{ nm}$  was chosen because no significant variations of the LIPSS patterns were observed for larger values. The lower limit  $\Delta_{\text{ablation}} = 20 \text{ nm}$  is related to the size of the Yee cells,  $\Delta x = \Delta y = 20 \text{ nm}$ . When  $\Delta_{\text{ablation}} < 20 \text{ nm}$ , HSFLs with extremely small periodicities seem able to grow. However, insufficient grid points are available to handle such small dimensions correctly in that case. The range of electron densities  $N_e$  was selected according to the previous studies of Bonse *et al.* with the Sipe-Drude model.<sup>7</sup>

Six regions can be identified on the map: LSFLs, LSFLs + Grooves, LSFLs + HSFLs  $\perp$ , HSFLs  $\perp$ , HSFLs  $\parallel$ , and “Mix.” HSFLs  $\perp$  and HSFLs  $\parallel$  refer to HSFLs orthogonal and parallel to the polarization of the laser radiation, respectively. Inset pictures which are representative of each region of the map have been included for the sake of clarity, except for the “Mix” region which is discussed in Sec. III E. It is important to stress that this map is compiled with the observations made after nine FDTD-feedback cycles. A map of the early stages would be more complex as can be extrapolated from the supplementary material (movies a.mp4 to e.mp4).<sup>34</sup> These movies show the evolution of the rough surfaces, through the nine FDTD-feedback cycles, for each inset picture of Fig. 3.

For high excitation states and relatively large  $\Delta_{\text{ablation}}$ , LSFLs, see Fig. 3(d) and movie d.mp4,<sup>34</sup> and LSFLs + Grooves, see Fig. 3(c) and movie c.mp4,<sup>34</sup> are the dominant kind of LIPSSs. For low excitation states, HSFLs parallel to the polarization, see Fig. 3(e) and movie e.mp4,<sup>34</sup> were observed, independently of  $\Delta_{\text{ablation}}$ . Interestingly, these are the only three kinds of LIPSSs which were reported in literature for silicon machined with  $\lambda = 800 \text{ nm}$  femtosecond lasers.<sup>7,14,19,35,36</sup> This can be explained by recalling that  $N_e$

and  $\Delta_{\text{ablation}}$  are decoupled in the HAM. It seems that silicon can hardly be processed in the low  $\Delta_{\text{ablation}}$  regime.

LSFLs are the most common kind of LIPSSs. Their periodicity in Figs. 3(c) and 3(d) is  $\Lambda = 738 \pm 21 \text{ nm}$  and  $\Lambda = 655 \pm 40 \text{ nm}$ , respectively. This variation of periodicity, while being expected from the results of recent work,<sup>7,37</sup> is discussed in more detail in Sec. III B. It is worth noting that the LSFL region extends to the left of the dashed vertical line, which represents  $\text{Re}(\tilde{n}^*) = \text{Im}(\tilde{n}^*)$ . The current electromagnetic theories consider LSFLs to be a consequence of the propagation of surface plasmon polaritons (SPPs), which can only occur when  $\text{Re}(\tilde{n}^*) < \text{Im}(\tilde{n}^*)$ .<sup>7,37</sup> Within the framework of these FDTD-feedback simulations, the propagation of SPPs is not a requirement for LSFL initiation and growth.

Concerning the grooves, that is, the “stripes” running parallel to the laser polarization in Fig. 3(c), their periodicity  $\Lambda$  is not well defined. That is,  $1.5 \mu\text{m} \leq \Lambda \leq 3.3 \mu\text{m}$  in Fig. 3(c). Interestingly, the orientation and range of periodicity match the characteristics of the grooves observed by Bonse and Krüger.<sup>36</sup> After nine FDTD-feedback cycles, LSFLs are still the dominant phenomenon under these conditions. In Fig. 3(c), grooves are present as boundaries where the LSFL pattern shows a disconnection. It seems that the grooves need a more accurate modeling of inter-pulse feedback mechanisms to “outgrow” LSFLs.

The occurrence of HSFLs orthogonal to the polarization, as can be observed in Fig. 3(a) and movie a.mp4,<sup>34</sup> is the most striking result of the FDTD-feedback simulations. While LSFLs and HSFLs parallel to the polarization can be predicted by the Sipe theory, HSFLs orthogonal to the polarization received few explanations.<sup>13,15–17</sup> The self-organization model proposed by Reif *et al.*<sup>16,17</sup> cannot predict a direct relation between the periodicity of LIPSSs and the wavelength of the laser radiation while the electromagnetic based approaches involve SHG,<sup>13,15</sup> which explains HSFL formation only in certain cases. According to Fig. 3, HSFLs orthogonal to the polarization occur for small  $\Delta_{\text{ablation}}$  and a large range of excitation states. However, these are more likely to develop for “moderate” excitation states. Qualitatively, small  $\Delta_{\text{ablation}}$  can be related to materials which are hard to deform. Sapphire,<sup>13</sup> titanium nitride, or diamond-like carbon<sup>12</sup> are hard materials which exhibit HSFLs very similar to the predictions of the FDTD-feedback simulations, for example. Interestingly, a small value of  $\Delta_{\text{ablation}}$  can be achieved easily with femtosecond lasers, while nanosecond lasers tend to remove or affect thicker layers of the material. This provides an explanation for the absence of HSFLs after nanosecond laser processing. The periodicity  $\Lambda$  of HSFLs in Fig. 3(a) is  $\Lambda = 125 \pm 13 \text{ nm}$ , which is  $0.14\lambda \leq \Lambda \leq 0.17\lambda$ , and is in the range of experimentally found periodicities of HSFLs in literature.<sup>12,13</sup> The variation of the characteristics of HSFLs is discussed in more detail in Sec. III C.

HSFLs orthogonal to the polarization can also be found superimposed on LSFLs after 9-FDTD feedback cycles, as can be observed in Fig. 3(b). This superposition of LIPSSs (denoted as LSFLs + HSFLs  $\perp$ ) acts like a transition zone between HSFLs orthogonal to the polarization and LSFLs. How pronounced the LSFLs and HSFLs are in the space

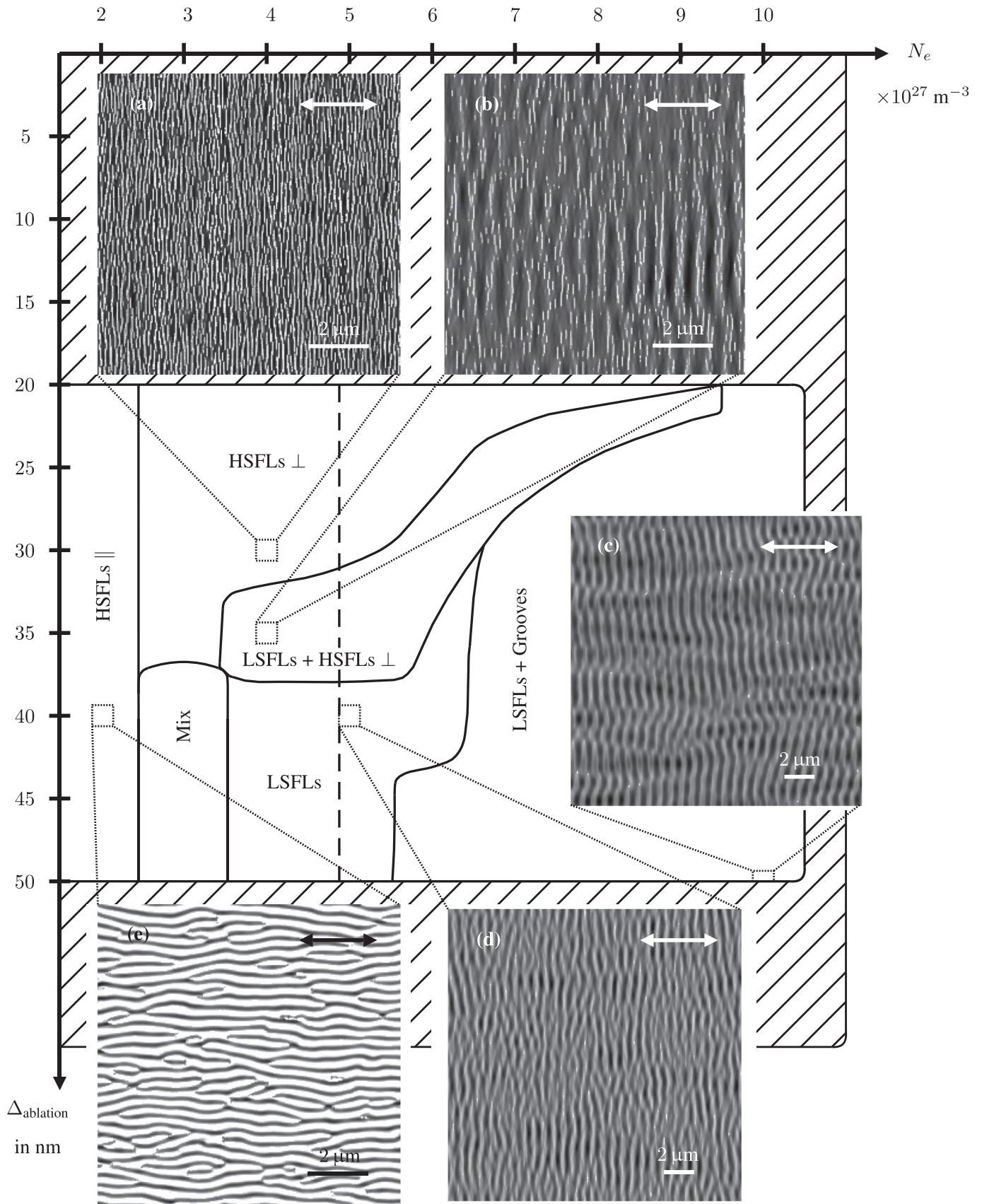


FIG. 3. Overview of the LIPSSs observed after nine FDTD-feedback cycles as function of  $N_e$  and  $\Delta_{\text{ablation}}$ , using the optical properties of excited silicon described in Sec. II A. The hatched regions indicate the sets of parameters without simulation results. The white arrows indicate the polarization direction of the laser radiation. The dashed vertical line represents  $\text{Re}(\tilde{n}^*) = \text{Im}(\tilde{n}^*)$ .

domain depends on the set of parameters ( $N_e$ ,  $\Delta_{\text{ablation}}$ ). Experimentally, such a superposition of LIPSSs was reported by Yao *et al.* on stainless steel and nickel for example.<sup>38</sup> Interestingly, LSFLs grew first, before being covered by HSFLs, in agreement with the FDTD-feedback simulations, see movie b.mp4.<sup>34</sup> It is worth noting that Yao *et al.* already proposed an electromagnetic explanation for the formation of these HSFLs, by studying locally the electromagnetic field distribution.<sup>38</sup>

HSFLs parallel to the polarization of the laser radiation “grow” in the FDTD-feedback simulations in the regime corresponding to a low excitation of silicon, as can be observed in Fig. 3(e) and movie e.mp4.<sup>34</sup> Their periodicity is  $\Lambda = 337 \pm 20$  nm. Costache *et al.* reported the presence of HSFLs on silicon, in the same direction as predicted by the present model.<sup>14</sup> However, they measured a smaller periodicity of  $\Lambda \approx 200$  nm. This discrepancy in periodicity is significant, but the LIPSSs observed by Costache *et al.* were produced with a number of 60 000 laser pulses, much larger than the nine FDTD-feedback cycles. This difference in number of “pulses” can be the cause of a variation in  $\Lambda$ . In addition, it is questionable if the LIPSSs observed by Costache *et al.* grow under conditions where ablation is the dominant process, since very small fluence levels were involved in their work. In this case, the HAM is probably not suited to model the formation of HSFLs parallel to the polarization correctly. This is further supported by looking at the movie e.mp4,<sup>34</sup> where the positions of HSFLs parallel to the polarization shift of about half of their period in the y direction, making them “oscillate.” This shift occurs because, on the contrary to LSFLs and HSFLs orthogonal to the polarization (see Secs. III B and III C), the minima and maxima of the absorbed energy profiles correspond to the valleys and the tops of the HSFLs, respectively. Hence, the valleys become the tops, and the tops the valleys, when material is “ablated” in these simulations. The “melting and expansion” of the regions with the highest absorbed energy values would be more realistic.

## B. Variation of the periodicity of LSFLs

The formation of LSFLs with a periodicity  $\Lambda$  slightly smaller than the laser wavelength  $\lambda$  is a recurrent topic in literature. Bonse et Krüger gathered three possible explanations for the periodicity of LSFLs being smaller than the laser wavelength ( $\Lambda \leq \lambda$ ).<sup>36</sup> First, the periodicity of SPPs depends on the optical properties of materials.<sup>7,37</sup> Since the optical properties can vary with the excited states of the material (number of electrons in the conduction band of semiconductors and dielectrics), different fluences lead to different optical properties, hence to different periodicities of SPPs. This assertion is discussed in more details in the next paragraph. Second, the periodicity of SPPs is affected by the presence of gratings, LSFLs in this case. According to Huang *et al.*,<sup>37</sup> the grating like LSFLs deepen with an increasing number of pulses applied, and this deepening leads to a decrease of the phase velocity of SPPs<sup>39</sup> therefore to a decreased periodicity of the interference pattern. This scenario suggests that the whole surface region containing

LSFLs melts and new LSFLs with a smaller periodicity form. This is in apparent disagreement with the cross-section study of Borowiec *et al.*, see Fig. 3 in Ref. 31, in which only a small resolidified layer of material is visible, mostly on top of LSFLs. Likewise, the combination of the FDTD calculations with the HAM does not support the grating-assisted variation of the periodicity of LSFLs, see movies c.mp4 and d.mp4.<sup>34</sup> That is, once LSFLs start to grow, the positions of their ridges do not shift<sup>40</sup> because the absorbed energy profile follows the surface morphology. Indeed, the smallest and largest values of the absorbed energy profile are aligned with the tops and the valleys of the LSFLs, respectively. Third, the periodicity of LSFLs is affected by the angle of incidence.<sup>6</sup> When enough pulses have been applied to form an ablation “crater,” the local angle of incidence on the “walls” of the crater can play a role. This last assertion is out of the scope of this article.

In Fig. 4, the periodicity  $\Lambda$  of LSFLs is presented as a function of the excitation level  $N_e$ , after nine FDTD-feedback cycles. The solid and dotted lines correspond to simulations performed with  $\Delta_{\text{ablation}} = 50$  nm and  $\Delta_{\text{ablation}} = 30$  nm, respectively. For  $\Delta_{\text{ablation}} = 50$  nm, besides the decrease of periodicity observed at  $N_e = 6 \times 10^{27} \text{ m}^{-3}$  ( $\tilde{n}^* = 1.436 + 2.255j$ ), the periodicity of LSFLs increases with increasing  $N_e$ , from  $\Lambda = 668 \pm 23$  nm for  $N_e = 4 \times 10^{27} \text{ m}^{-3}$  ( $\tilde{n}^* = 1.943 + 1.116j$ ) to  $\Lambda = 738 \pm 21$  nm for  $N_e = 10 \times 10^{27} \text{ m}^{-3}$  ( $\tilde{n}^* = 1.348 + 3.993j$ ). The smallest value  $\Lambda = 662 \pm 23$  nm of the solid curve is reached for  $N_e = 6 \times 10^{27} \text{ m}^{-3}$ , while it was expected for  $N_e = 4 \times 10^{27} \text{ m}^{-3}$ . This phenomenon may be attributed to the chosen random roughness, being more or less favorable to certain excitation states (it may also be simply in the range of the error bars). For a smaller ablation depth  $\Delta_{\text{ablation}} = 30$  nm, the periodicity of LSFLs is only slightly smaller than in the case of  $\Delta_{\text{ablation}} = 50$  nm, when  $N_e > 6 \times 10^{27} \text{ m}^{-3}$ . The case of  $N_e = 6 \times 10^{27} \text{ m}^{-3}$ , for  $\Delta_{\text{ablation}} = 30$  nm, is special. Here, the periodicity of LSFLs,  $\Lambda = 601 \pm 69$  nm, is the smallest of Fig. 4 and the measurement shows the largest error bar (standard deviation of the measured periodicities). The cause of these

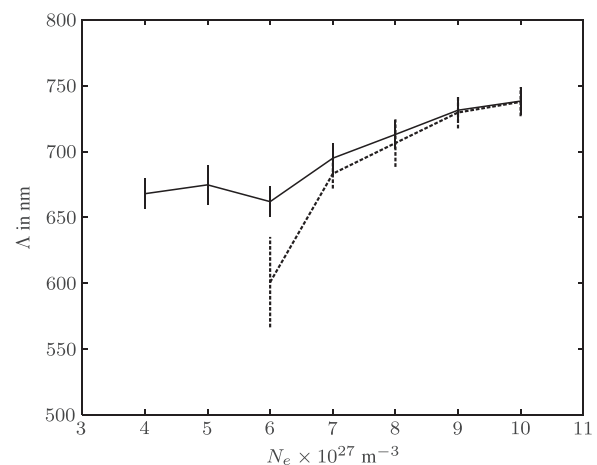


FIG. 4. Periodicity  $\Lambda$  of LSFLs after nine FDTD-feedback cycles as a function of the number of electrons in the conduction band  $N_e$ . The solid and dotted lines correspond to simulations performed with  $\Delta_{\text{ablation}} = 50$  nm and  $\Delta_{\text{ablation}} = 30$  nm, respectively. The error bars indicate the standard deviation of the periodicities measured in the  $20 \times 20 \mu\text{m}^2$  areas.



observations is the presence of HSFLs, orthogonal to the polarization of the laser radiation, on top of some LSFLs, as expected from Fig. 3.

It is worth noting that, excluding the case of  $N_e = 6 \times 10^{27} \text{ m}^{-3}$  and  $\Delta_{\text{ablation}} = 30 \text{ nm}$ , the results of the FDTD-feedback simulations are in good agreement with the results of the Sipe-Drude model for silicon.<sup>7</sup> That is, the periodicities predicted are larger than 650 nm and smaller than the laser wavelength. However, this prediction alone does not allow to explain all the experimental observations. Indeed, for a number of pulses  $N$  smaller or equal than 10, the periodicities reported by Bonse and Krüger<sup>36</sup> are in the range of  $650 \text{ nm} \leq \Lambda \leq 800 \text{ nm}$ , while for larger number of pulses,  $N \geq 100$ , the periodicities decrease to  $\Lambda \approx 500\text{--}600 \text{ nm}$ . In the Sipe-Drude model, the periodicities of LSFLs are estimated from the location of the features related to SPPs in the frequency domain. Likewise, Huang *et al.* use SPPs, outside the framework of the Sipe theory, to explain the characteristics of LSFLs.<sup>37</sup> When the periodicities become too small (i.e.,  $\Lambda \leq 650 \text{ nm}$ ), these theories fail and the grating-assisted SPPs theory was proposed.<sup>36,37</sup> As discussed previously, the cross-section study of Borowiec *et al.*,<sup>31</sup> along with the combination of the FDTD calculations with the HAM, does not support the grating-assisted variation of the periodicity of LSFLs. Instead, the results of the FDTD-feedback simulations suggest that these LSFLs are, in fact, a mix of LSFLs and HSFLs. The onset of such a mix can be observed in Fig. 3(d). The LIPSSs in Fig. 3(d) were classified as “LSFLs” in the overview map, because LSFLs dominate the space domain for these conditions. However, one can observe several LSFLs splitting into smaller LIPSSs. This is easily noticed when Fig. 3(c) and Fig. 3(d) are compared. It is worth noting that this mix of LSFLs and HSFLs is different from the one presented in Fig. 3(b).

To summarize this section, it is proposed here that the variation of the periodicity of LSFLs has three causes. The first cause is related to the variation of the periodicity of SPPs, when they are present, as proposed by Bonse *et al.*<sup>7</sup> The second cause involves the presence of a mix of LSFLs and HSFLs. The occurrence of these two mechanisms is directly linked to the fluence applied, which governs the excitation state of the material. The third cause concerns the influence of the local angle of incidence on the periodicity of LSFLs,<sup>7</sup> which was not discussed here.

### C. Variation of the properties of HSFLs $\perp$

HSFLs orthogonal to the polarization of the laser radiation are not as regular as LSFLs. Therefore, their characteristics are harder to describe. Indeed, the properties of HSFLs can vary significantly, as shown in Fig. 5. In Figs. 5(a)–5(c), three kinds of HSFLs orthogonal to the polarization, and their respective Fourier transform, in Figs. 5(d)–5(f), are presented. For the sake of clarity, only  $5 \times 5 \mu\text{m}^2$  regions of the simulated  $20 \times 20 \mu\text{m}^2$  surfaces are shown. However, the Fourier transform was applied to the  $20 \times 20 \mu\text{m}^2$  areas.

As can be observed in the space domain, HSFLs show variations of width (lateral dimension), density (number of HSFLs per  $\mu\text{m}^2$ ) and length (vertical dimension). In Fig. 5(a), HSFLs are wide, long, and closely packed, in contrary

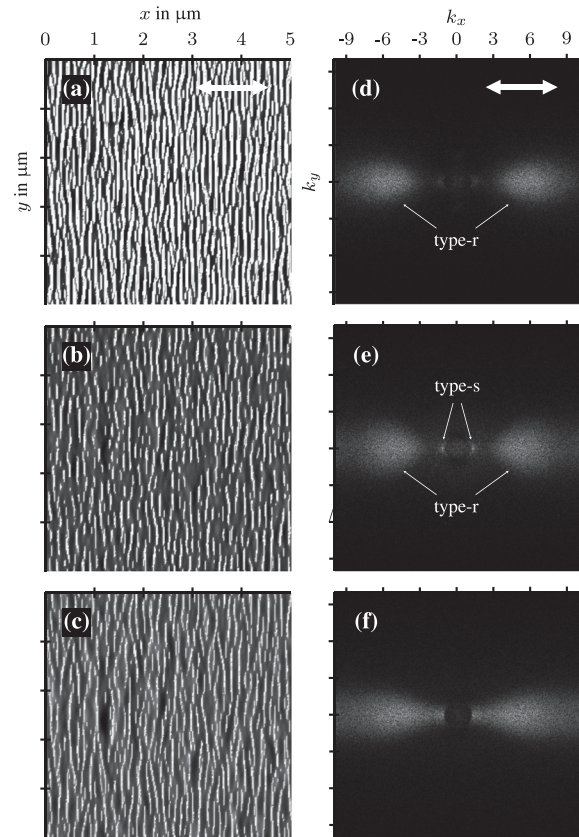


FIG. 5.  $5 \times 5 \mu\text{m}^2$  areas covered with HSFLs (left column) and their Fourier transforms (right column), obtained under different simulation conditions. (a)  $N_e = 3 \times 10^{27} \text{ m}^{-3}$  ( $\bar{n}^* = 2.401 + 0.679j$ ),  $\Delta_{\text{ablation}} = 30 \text{ nm}$ , and nine FDTD-feedback cycles. (b)  $N_e = 4 \times 10^{27} \text{ m}^{-3}$  ( $\bar{n}^* = 1.943 + 1.116j$ ),  $\Delta_{\text{ablation}} = 30 \text{ nm}$ , and seven FDTD-feedback cycles. (c)  $N_e = 6 \times 10^{27} \text{ m}^{-3}$  ( $\bar{n}^* = 1.436 + 2.255j$ ),  $\Delta_{\text{ablation}} = 25 \text{ nm}$ , and nine FDTD-feedback cycles. (d), (e), and (f) are the Fourier transforms related to (a), (b), and (c) respectively. The white arrows indicate the direction of the polarization of the laser radiation. The vector  $\vec{k} = (k_x, k_y)$  spanning the frequency domain is normalized by the norm of the laser wave vector,  $2\pi/\lambda$ . The y scale is identical to the x scale.

to Fig. 5(b), where HSFLs are thin, short, and relatively spaced. It is also possible to obtain them thin, long, and closely packed in Fig. 5(c). As a result, these HSFLs cannot be fully characterized by a single well defined periodicity.

The same can be concluded from the frequency domain analysis. In the following, the notations used in previous frequency domain studies of LIPSSs are employed.<sup>18,21</sup> That is, the notations “LSFLs” and “HSFLs” refer to the space domain, while “type-s features” or “type-r features” are used to refer to characteristics in the frequency domain. The type-r features in Fig. 5(d) are less spread than in Fig. 5(e) or Fig. 5(f), leading to long wide HSFLs in the space domain.

In Fig. 5(e), the type-s features, usually related to the presence of LSFLs, become visible. The type-r features are “larger” (i.e., more spread) in the  $k_y$  direction than in Fig. 5(d), which hinders the regularity of the HSFLs. Finally, the type-r features spread in the  $k_x$  direction and merge with the type-s features in Fig. 5(f). Hence, many frequencies contribute to the profile of HSFLs in Fig. 5(c), making them thin. While the type-r location is closer to  $(k_x, k_y) = (0, 0)$  than in Fig. 5(d), for example, the large spread of the type-r features along  $k_x$  triggers closely packed HSFLs in the space domain.

It is worth noting that Figs. 5(d)–5(f) show three kinds of frequency “arrangements” leading to HSFLs in the space domain. Indeed, the type-s features can be almost absent, as in Fig. 5(d), present and distinct from the type-r features, as in Fig. 5(e), or merged with the type-r features, as in Fig. 5(f). This panel of possibilities, and the strong dependence of the location and spread of the type-r features on  $(N_e, \Delta_{\text{ablation}})$ , is in agreement with what is reported in literature. That is, HSFLs orthogonal to the polarization have been reported with large variations of their properties, mainly in terms of periodicity. Moreover, the HSFLs orthogonal to the polarization, which develop in the FDTD-feedback simulations, show large aspect ratios: the heights of the HSFLs get larger than the widths of the HSFLs, as reported in certain cases.<sup>29,30</sup> This occurs because the absorbed energy profiles have their maxima aligned with the valleys of the HSFLs, while their minima are aligned with the tops.

The type-r features can explain the formation of certain HSFLs orthogonal to the polarization. Indeed, the HSFLs orthogonal to the polarization, which grow in the FDTD-feedback simulations, resemble some of the HSFLs reported in literature.<sup>12,13,41</sup> Nevertheless, the presence of certain HSFLs orthogonal to the polarization found other explanations, such as SHG<sup>13,15</sup> or self-organization,<sup>16,17</sup> which are not invalidated by the present simulations. It is worth noting that Borowiec and Haugen established a one photon transparency requirement for the growth of HSFLs orthogonal to the polarization on semiconductors and dielectrics.<sup>13</sup> Bonse *et al.* showed that it is not always necessary,<sup>41</sup> which is corroborated by the FDTD-feedback simulations. However, being in a regime where the material is “transparent” seems beneficial, see the position of the “HSFLs  $\perp$ ” area, mainly of the left of the dashed line in Fig. 3. Studies of the frequency domain spectrum of HSFLs orthogonal to the polarization, and of LIPSSs in general (see Sec. III F), should allow to identify their origin without ambiguity.

#### D. HSFLs parallel to the polarization on metals

According to Fig. 3, HSFLs parallel to the polarization form only when  $\text{Re}(\tilde{n}^*) > \text{Im}(\tilde{n}^*)$ . However, HSFLs parallel to the polarization were observed on alloyed steel<sup>3</sup> and titanium,<sup>4</sup> for example.

In Fig. 6,  $5 \times 5 \mu\text{m}^2$  areas, extracted from the  $20 \times 20 \mu\text{m}^2$  simulated surfaces, are presented, along with the logarithm of the amplitude of their corresponding Fourier transforms. Presenting the Fourier transforms logarithmically allows to observe the presence of frequencies with small amplitudes compared to the maximum.

The three space domain figures, Figs. 6(a)–6(c), present nets of “stripes.” The stripes parallel to the polarization can be observed when  $\text{Re}(\tilde{n}^*) > \text{Im}(\tilde{n}^*)$ , Fig. 6(a), as well as when  $\text{Re}(\tilde{n}^*) < \text{Im}(\tilde{n}^*)$ , Figs. 6(b) and 6(c). However, their presence requires relatively small  $\Delta_{\text{ablation}}$  when the excitation state gets high, along with a small number of FDTD-feedback cycles, 3 here. It is worth noting that what is presented in Fig. 6 occurs at an earlier stage than what is presented in Fig. 3.

The characteristics of these stripes parallel to the polarization can vary significantly, in terms of density, periodicity

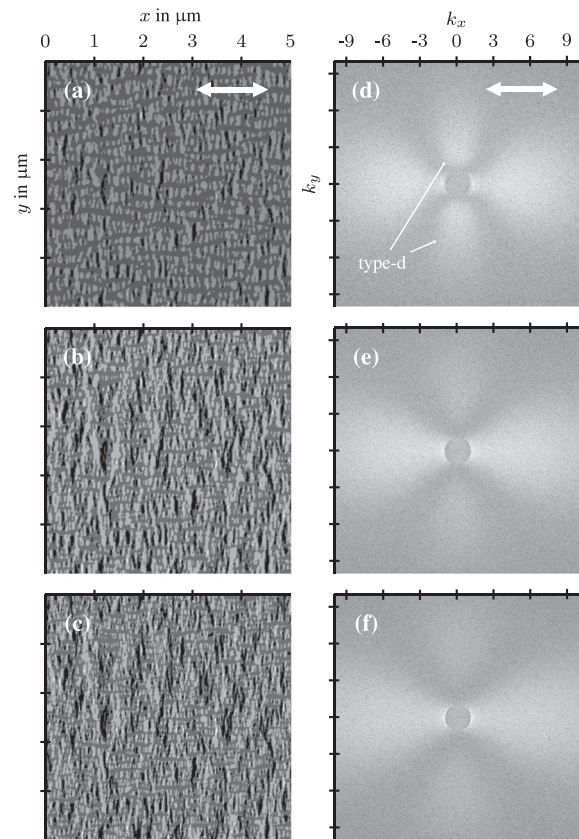


FIG. 6.  $5 \times 5 \mu\text{m}^2$  areas (left column), obtained under different simulation conditions, and the logarithm of the amplitude of their Fourier transforms (right column). (a)  $N_e = 4 \times 10^{27} \text{m}^{-3}$  ( $\tilde{n}^* = 1.943 + 1.116j$ ),  $\Delta_{\text{ablation}} = 30 \text{nm}$ , and three FDTD-feedback cycles. (b)  $N_e = 6 \times 10^{27} \text{m}^{-3}$  ( $\tilde{n}^* = 1.436 + 2.255j$ ),  $\Delta_{\text{ablation}} = 25 \text{nm}$ , and three FDTD-feedback cycles. (c)  $N_e = 8 \times 10^{27} \text{m}^{-3}$  ( $\tilde{n}^* = 1.339 + 3.220j$ ),  $\Delta_{\text{ablation}} = 20 \text{nm}$ , and three FDTD-feedback cycles. (d), (e), and (f) are the Fourier transforms related to (a), (b), and (c) respectively. The white arrows indicate the direction of the polarization of the laser radiation. The vector  $\vec{k} = (k_x, k_y)$  spanning the frequency domain is normalized by the norm of the laser wave vector,  $2\pi/\lambda$ . The y scale is identical to the x scale.

and width. In Fig. 6(a), the stripes are wide and dense, mainly because they merge in the horizontal direction. They are also better defined (sharper) than in Figs. 6(b) and 6(c). In Figs. 6(b) and 6(c), the stripes are less wide and less extended in the horizontal direction. The periodicity is also slightly smaller than in Fig. 6(a), which is more easily concluded from the frequency domain. Naturally, the Fourier transforms are in agreement with the space domain observations. That is, the type-d features have a larger amplitude in Fig. 6(a) than in Figs. 6(b) and 6(c). The type-d features are at larger  $k_y$  and more spread in the  $N_e = 6 \times 10^{27} \text{m}^{-3}$  (Fig. 6(e)) and  $N_e = 8 \times 10^{27} \text{m}^{-3}$  (Fig. 6(f)) cases. As for the HSFLs orthogonal to the polarization, the parallel stripes cannot be fully characterized by a single periodicity value.

Apart from these stripes parallel to the polarization of the laser radiation, HSFLs parallel to the polarization do not grow in the FDTD-feedback simulations when  $\text{Re}(\tilde{n}^*) < \text{Im}(\tilde{n}^*)$ . Experimentally, these HSFLs grow on metals irradiated at low fluence levels compared to LSFLs.<sup>3,4</sup> As mentioned previously, the HAM seems to fail at describing properly regimes where the molten state of the material plays a role. This is not surprising, considering the “ablative”



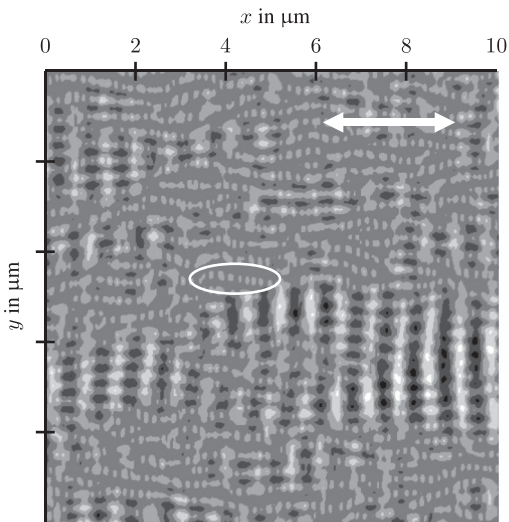


FIG. 7. Mixed LIPSS pattern after five FDTD-feedback cycles. The simulations were performed for  $N_e = 3 \times 10^{27} \text{ m}^{-3}$  ( $\tilde{n}^* = 2.401 + 0.679j$ ) and  $\Delta_{\text{ablation}} = 50 \text{ nm}$ . A grayscale colomap, where the white color represents the largest values, is used to represent the rough surface. The polarization direction is indicated by the white arrow. The y scale is identical to the x scale.

nature of the HAM. Nonetheless, the FDTD-feedback simulations show that HSFLs parallel to the polarization, growing on metals, can be understood in the frame of an electromagnetic approach.

### E. Superposition of LIPSSs

The prediction of the “Mix” region in Fig. 3 is one of the striking results of the FDTD-feedback simulations. In Fig. 7, a complex LIPSS pattern can be observed. This surface topography was obtained after five FDTD-feedback cycles,  $N_e = 3 \times 10^{27} \text{ m}^{-3}$  and  $\Delta_{\text{ablation}} = 50 \text{ nm}$ . This simulation result was selected because it shows the best how the type-s, type-d, and type-r features can jointly contribute to the space

domain profile. Their combined “fingerprints” in the space domain can lead to a kind of “superposition” of LIPSSs.

The superposition of LIPSSs, as presented in Fig. 7, was not reported in the literature for  $\lambda = 800 \text{ nm}$ . However, Crawford and Haugen observed a kind of LIPSSs with  $\Lambda \ll \lambda$ , referred to as “fine bumps,” on silicon.<sup>42</sup> They were produced at rather large wavelengths (about 1300 nm and about 2100 nm) compared to the wavelength of experiments at  $\lambda = 800 \text{ nm}$ , typical for fs lasers. The array of dots present in the FDTD-feedback simulations (white ellipse in Fig. 7) offers the possibility to explain the formation of these fine bumps. The fact that this regime exists in the FDTD-feedback simulations, performed with  $\lambda = 800 \text{ nm}$ , is probably due to the decoupling of  $N_e$  and  $\Delta_{\text{ablation}}$  discussed in Sec. II C.

It is worth noting that the case where  $N_e = 3 \times 10^{27} \text{ m}^{-3}$  is particularly important in the FDTD-feedback simulations, since it shows that an electromagnetic approach can account for the formation of mixed LIPSS patterns while the formation of these patterns was considered to be supporting the self-organization theory.<sup>16</sup>

### F. Overview of the frequency domain features

In Fig. 8, the Fourier transforms which are characteristic of the LIPSS regions presented in Fig. 3 are shown. One major difference with Fig. 3 is that not all the results were obtained after nine FDTD-feedback cycles. The main reason is that certain frequencies are easily concealed by others. In particular, the type-s features tend to dominate the frequency domain after nine FDTD-feedback cycles, while other LIPSSs can be observed in the space domain.

Figure 8(a) is the most common frequency domain representation of LIPSSs, which is already known from the Sipe theory.<sup>11</sup> Bonse *et al.* studied the type-s properties extensively to explain the variation of characteristics of LSFLs.<sup>7</sup> The exact position and spread of the type-s features depend

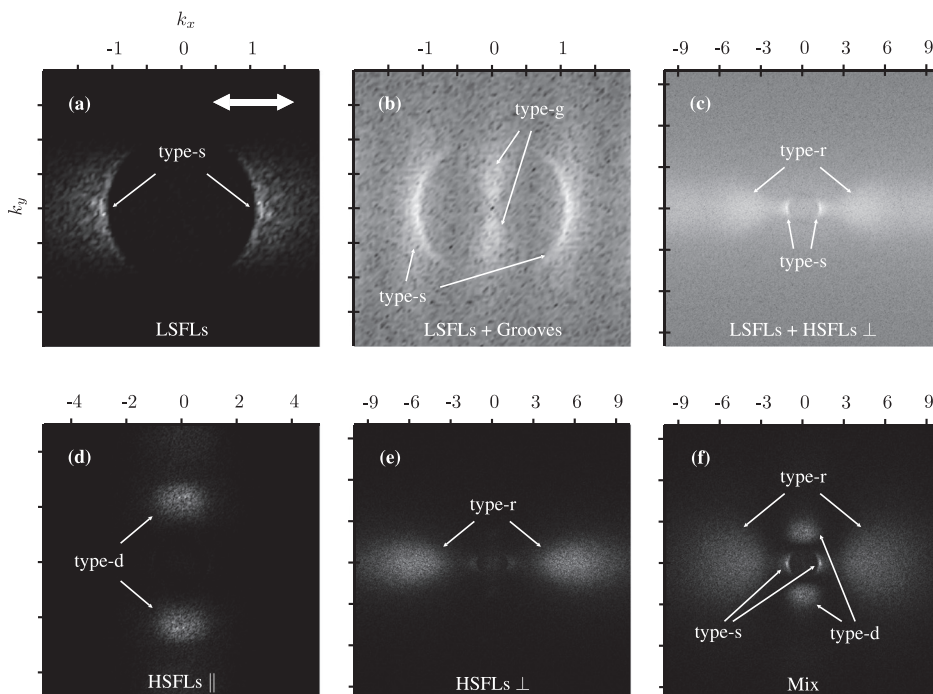
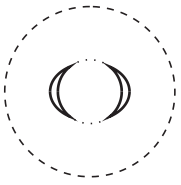
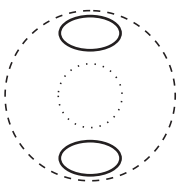
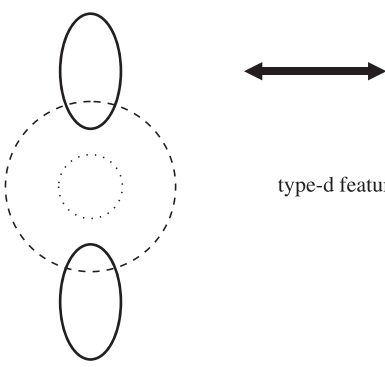
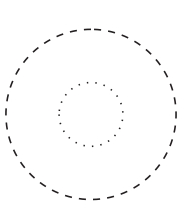
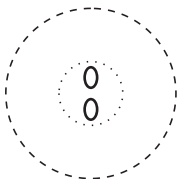


FIG. 8. Overview of the signature of LIPSSs in the frequency domain. The number of FDTD-feedback cycles is 9 in all cases, except for (a) and (f), where six and three cycles are used, respectively. ( $N_e$ ,  $\Delta_{\text{ablation}}$ ) are indicated without “ $\times 10^{27} \text{ m}^{-3}$ ” and “nm,” respectively, for each subfigure. (a) (5,50), (b) (10,30), (c) (4,35), (d) (2,20), (e) (3,30), and (f) (3,35). The vector  $\vec{k} = (k_x, k_y)$  spanning the frequency domain is normalized by the norm of the laser wave vector,  $2\pi/\lambda$ . The y scale is identical to the x scale.

TABLE I. Summary of the different LIPSSs predicted by the FDTD-feedback simulations along with their signature in the frequency domain. The dotted and dashed circles indicate  $\|\vec{k}\| = 1$  and  $\|\vec{k}\| = \text{Re}(\tilde{n}^*)$ , respectively.

LSFLs $\Lambda \leq \lambda, \perp$		type-s features
HSFLs $\Lambda \geq \lambda/\text{Re}(\tilde{n}^*), \parallel$		type-d features
HSFLs $\Lambda \ll \lambda, \parallel$		type-d features
HSFLs $\Lambda \ll \lambda, \perp$		type-r features
Grooves $\Lambda > \lambda, \parallel$		type-g features

on  $N_e$ ,  $\Delta_{\text{ablation}}$ , and the number of FDTD-feedback cycles in these simulations, as expected from the space domain discussion and Sec. III B.

In Fig. 8(b), the logarithm applied on the amplitude of the Fourier transform of a surface with LSFLs and grooves is shown. The existence of type-g features, where “g” stands for “grooves,” was already suggested in previous work<sup>18,21</sup> and is confirmed here. As mentioned in Sec. III A, it seems that feedback mechanisms are crucial for the growth of grooves. It is worth noting that without applying the logarithm, only the type-s features would be

observed. The same holds for Fig. 8(c), which is a Fourier transform, characteristic of the presence of HSFLs orthogonal to the polarization superimposed on LSFLs. As discussed in Sec. III C, the type-r features depends strongly on the depth and the excitation state of the material, meaning that HSFLs on top of LSFLs can show large variations of their properties. In the case of HSFLs on top of LSFLs, it is possible to observe the type-r features with roughly the same shape as the type-s features, but for  $\|k_x\| = 2$  (not shown here), which looks like frequency doubling.

The type-d features can be observed alone in Fig. 8(d). They are located for  $k_y$  slightly smaller than  $\text{Re}(\tilde{n}^*)$  here, which was also discussed in previous work.<sup>18</sup> However, it was shown in Sec. III D that their characteristics can differ from this usual description. These frequency domain features are related to the growth of HSFLs parallel to the polarization in the FDTD-feedback simulations.

The type-r features, in Fig. 8(e), are the signature of HSFLs orthogonal to the polarization in the frequency domain. They can conceal the other frequency domain features, even the type-s features. As discussed in Sec. III C, the exact location and shape of the type-r features depend strongly on the set  $(N_e, \Delta_{\text{ablation}})$ , which is in agreement with the fact that HSFLs orthogonal to the polarization show large variations of their characteristics in literature.

Interestingly, it is possible to observe three types of frequency domain features (out of four) jointly in Fig. 8(f). Inter-pulse feedback mechanisms do not always lead to a clear dominance of a specific kind of frequency domain features. The “fingerprints” in the space domain of such a frequency arrangement were discussed in Sec. III E.

#### IV. CONCLUSION

A new model predicting the formation of LIPSSs was presented. This model combines FDTD calculations, to study the interaction of electromagnetic waves with rough surfaces, and a simple non-physical ablation threshold to include inter-pulse feedback mechanisms, which is referred to as holographic ablation model. The results, referred to as FDTD-feedback simulations, show that the formation of LIPSSs can be understood in the frame of an electromagnetic theory. Indeed, LSFLs, HSFLs and, to a certain extent, grooves “grow” in the simulation domain.

Table I is a summary of the different LIPSSs predicted by these FDTD-feedback simulations, along with their signature in the frequency domain. LSFLs and the type-s features are modeled correctly, including their decrease in periodicity compared to the wavelength of the laser radiation. It was shown that the propagation of SPPs is not a sine qua non condition for LSFL formation. Moreover, the grating-assisted mechanism, proposed by other authors to explain the periodicity of LSFLs being smaller than  $\lambda$  in certain cases, seems inapplicable.

Grooves parallel to the polarization, related to the type-g features, were predicted by the model to occur jointly with LSFLs. Grooves without LSFLs were not found.

The growth of HSFLs parallel to the polarization of the laser radiation is also predicted by the present model. This was expected for semiconductors and dielectrics since the type-d features were already reported by the Sipe theory for this kind of materials. However, the FDTD-feedback simulations show that HSFLs parallel to the polarization can be expected on metals as well, in agreement with experimental results.

The most striking result of the FDTD-feedback simulations is the presence of HSFLs orthogonal to the polarization, related to the type-r features. Their periodicity can be small compared to the wavelength of the laser radiation and is expected to change significantly for varying material

properties. Although the optical properties of silicon have been used in the FDTD-feedback simulations presented here, the modeling results also contribute to a better understanding of LIPSS formation on other materials. Future work will be carried out to show that the different LIPSSs, in particular the HSFLs orthogonal to the polarization, are present experimentally, in agreement with their frequency domain signature as predicted by the model.

The FDTD-feedback simulations bring many answers regarding LIPSS formation; nevertheless, several improvements can be foreseen. First, the simulations were performed for linearly polarized plane waves, arriving at normal incidence on the rough surfaces of the media. A study at off-normal incidence, or with different polarization states, would be of interest, especially for the type-r features. Second, effects related to the Gaussian distribution of the fluence, provided by most laser sources, are not taken into account in the FDTD-feedback simulations. This hinders the comparison with experiments where several laser pulses, with a Gaussian fluence profile, are put at the same location on a sample. Third, the intra-pulse and inter-pulse feedback mechanisms need a better description to obtain fully quantitative results.

#### ACKNOWLEDGMENTS

This research was carried out under Project No. M61.3.08300 in the framework of the Research Program of the Materials innovation institute M2i ([www.m2i.nl](http://www.m2i.nl)).

<sup>1</sup>M. Birnbaum, *J. Appl. Phys.* **36**, 3688 (1965).

<sup>2</sup>Y. Jee, M. F. Becker, and R. M. Walsler, *J. Opt. Soc. Am. B* **5**, 648 (1988).

<sup>3</sup>A. J. Huis in't Veld and J. van der Veer, *J. Laser Micro/Nanoeng.* **5**, 28 (2010).

<sup>4</sup>J. Bonse, S. Höhm, A. Rosenfeld, and J. Krüger, *Appl. Phys. A* **110**, 547 (2013).

<sup>5</sup>D. C. Emmony, R. P. Howson, and L. J. Willis, *Appl. Phys. Lett.* **23**, 598 (1973).

<sup>6</sup>J. F. Young, J. S. Preston, H. M. van Driel, and J. E. Sipe, *Phys. Rev. B* **27**, 1155 (1983).

<sup>7</sup>J. Bonse, A. Rosenfeld, and J. Krüger, *J. Appl. Phys.* **106**, 104910 (2009).

<sup>8</sup>P. Temple and M. Soileau, *IEEE J. Quantum Electron.* **17**, 2067 (1981).

<sup>9</sup>Q. Wu, Y. Ma, R. Fang, Y. Liao, Q. Yu, X. Chen, and K. Wang, *Appl. Phys. Lett.* **82**, 1703 (2003).

<sup>10</sup>S. Kaneko, T. Ito, K. Akiyama, M. Yasui, C. Kato, S. Tanaka, Y. Hirabayashi, A. Mastuno, T. Nire, H. Funakubo, and M. Yoshimoto, *Nanotechnology* **22**, 175307 (2011).

<sup>11</sup>J. E. Sipe, J. F. Young, J. S. Preston, and H. M. van Driel, *Phys. Rev. B* **27**, 1141 (1983).

<sup>12</sup>N. Yasumaru, K. Miyazaki, and J. Kiuchi, *Appl. Phys. A: Mater. Sci. Process.* **76**, 983 (2003).

<sup>13</sup>A. Borowiec and H. K. Haugen, *Appl. Phys. Lett.* **82**, 4462 (2003).

<sup>14</sup>F. Costache, S. Kouteva-Arguirova, and J. Reif, *Appl. Phys. A: Mater. Sci. Process.* **79**, 1429 (2004).

<sup>15</sup>D. Dufft, A. Rosenfeld, S. K. Das, R. Grunwald, and J. Bonse, *J. Appl. Phys.* **105**, 034908 (2009).

<sup>16</sup>J. Reif, F. Costache, M. Henyk, and S. V. Pandelov, *Appl. Surf. Sci.* **197–198**, 891, (2002).

<sup>17</sup>J. Reif, O. Varlamova, S. Varlamov, and M. Besthorn, *Appl. Phys. A: Mater. Sci. Process.* **104**, 969 (2011).

<sup>18</sup>J. Z. P. Skolski, G. R. B. E. Römer, J. V. Obona, V. Ocelik, A. J. Huis in't Veld, and J. T. M. De Hosson, *Phys. Rev. B* **85**, 075320 (2012).

<sup>19</sup>M. Huang, F. Zhao, Y. Cheng, N. Xu, and Z. Xu, *Opt. Express* **18**, A600 (2010).

<sup>20</sup>K. Sokolowski-Tinten and D. von der Linde, *Phys. Rev. B* **61**, 2643 (2000).

<sup>21</sup>J. Z. P. Skolski, G. R. B. E. Römer, J. V. Obona, V. Ocelik, A. J. Huis in't Veld, and J. T. M. De Hosson, *J. Laser Micro/Nanoeng.* **8**, 1 (2013).

<sup>22</sup>K. S. Yee, *IEEE Trans. Antennas Propag.* **14**, 302 (1966).



- <sup>23</sup>A. Taflove and S. C. Hagness, *Computational Electrodynamics: The Finite-Difference Time-Domain Method*, 3rd ed. (Artech House, Norwood, MA, 2005).
- <sup>24</sup>A. Taflove and M. E. Brodwin, *IEEE Trans. Microwave Theory Tech.* **23**, 623 (1975).
- <sup>25</sup>J. A. Roden and S. D. Gedney, *Microwave Opt. Technol. Lett.* **27**, 334 (2000).
- <sup>26</sup>R. E. Mickens, *Advances in the Applications of Nonstandard Finite Difference Schemes* (World Scientific Publishing Company, 2005).
- <sup>27</sup>A. A. Kokhanovsky, *Light Scattering and Remote Sensing of Atmosphere and Surface, Light Scattering Reviews*, Vol. 6 (Springer, 2012).
- <sup>28</sup>J. F. Young, J. E. Sipe, and H. M. van Driel, *Phys. Rev. B* **30**, 2001 (1984).
- <sup>29</sup>E. M. Hsu, T. H. R. Crawford, C. Maunders, G. A. Botton, and H. K. Haugen, *Appl. Phys. Lett.* **92**, 221112 (2008).
- <sup>30</sup>T. Tomita, R. Kumai, S. Matsuo, S. Hashimoto, and M. Yamaguchi, *Appl. Phys. A: Mater. Sci. Process.* **97**, 271 (2009).
- <sup>31</sup>A. Borowiec, M. Couillard, G. A. Botton, and H. K. Haugen, *Appl. Phys. A: Mater. Sci. Process.* **79**, 1887 (2004).
- <sup>32</sup>O. Varlamova, M. Bounhalli, and J. Reif, *Appl. Surf. Sci.* **278**, 62 (2013).
- <sup>33</sup>J. Bonse, J. M. Wrobel, J. Krüger, and W. Kautek, *Appl. Phys. A: Mater. Sci. Process.* **72**, 89 (2001).
- <sup>34</sup>See supplementary material at <http://dx.doi.org/10.1063/1.4867759> for movies showing the formation of HSFLs  $\perp$ , LSFLs+HSFLs  $\perp$ , LSFLs+Grooves, LSFLs, and HSFLs  $\parallel$ .
- <sup>35</sup>J. Bonse, S. Baudach, J. Krüger, W. Kautek, and M. Lenzner, *Appl. Phys. A: Mater. Sci. Process.* **74**, 19 (2002).
- <sup>36</sup>J. Bonse and J. Krüger, *J. Appl. Phys.* **108**, 034903 (2010).
- <sup>37</sup>M. Huang, F. L. Zhao, Y. Cheng, N. Xu, and Z. Xu, *ACS Nano* **3**, 4062 (2009).
- <sup>38</sup>J. W. Yao, C. Y. Zhang, H. Y. Liu, Q. F. Dai, L. J. Wu, S. Lan, A. V. Gopal, V. A. Trofimov, and T. M. Lysak, *Opt. Express* **20**, 905 (2012).
- <sup>39</sup>H. Raether, *Surface Plasmons on Smooth and Rough Surfaces and on Gratings* (Springer-Verlag, 1988).
- <sup>40</sup>An experimental study of the pulse to pulse formation of LSFLs will be published; J. Vincenc Obona, J. Z. P. Skolski, G. R. B. E. Römer, and A. J. Huis in't Veld, "Pulse-analysis-pulse investigation of femtosecond laser-induced periodic surface structures on silicon in air," *Opt. Express* (submitted).
- <sup>41</sup>J. Bonse, M. Munz, and H. Sturm, *J. Appl. Phys.* **97**, 013538 (2005).
- <sup>42</sup>T. H. R. Crawford and H. K. Haugen, *Appl. Surf. Sci.* **253**, 4970 (2007).